

A multiscale approach for quantitative simulations of diffusion induced segregation

T Blesgen

Max-Planck-Institute for Mathematics in the Sciences, Inselstrasse 22, 04103 Leipzig, Germany

E-mail: blesgen@mis.mpg.de

Received 24 August 2005, in final form 14 February 2006

Published 9 March 2006

Online at stacks.iop.org/MSMSE/14/389

Abstract

In this paper quantitative simulations of a particular segregation problem arising in mineralogy are done. Using *ab initio* methods, in particular, the harmonic approximation, the free energy of the physical process is calculated for a range of concentration vectors. Furthermore, diffusion coefficients and elasticity coefficients are computed. The obtained data are the foundation for high-precision finite element computations. For selected configurations, the computed free energies are validated with results from quantum mechanics.

(Some figures in this article are in colour only in the electronic version)

1. Introduction

The present work is concerned with computer simulations on the so-called chalcopyrite disease within sphalerite. This is a well-known and extensively-discussed problem arising in geology. The quantitative description of this process helps to get a precise understanding of the time scales involved in magma ascending from the earth's core and might lead to better predictions of earthquakes and volcanic eruptions.

A characteristic of chalcopyrite disease is the presence of a melon-type structure close to the boundary of a rock sample (figure 1).

The common understanding is that these structures develop during a long time period in the range of several hundred thousand years. Since no experimentalist would be so patient, mineralogists studied chalcopyrite disease under altered conditions in the laboratory, where they surrounded a ZnS single crystal with sulfur gas, spread copper powder on its surface and significantly increased the temperature (kept isothermally between $T = 550^\circ\text{C}$ and $T = 700^\circ\text{C}$); see the reports of the experiments [3, 4]. With an increase in T (and sufficiently high sulfur fugacity, see below) the process is accelerated and the characteristic pattern formation is observed after several weeks ($T = 700^\circ\text{C}$) or months ($T = 550^\circ\text{C}$).

Chalcopyrite disease is caused by gradients of the chemical potential induced by an increase in external sulfur fugacity. Hereby, the primary Fe^{2+} is oxidized to Fe^{3+} and reacts



Figure 1. Part of the boundary region of a rock sample with chalcopyrite disease (reflecting light image), black matrix: sphalerite, white grains: chalcopyrite.

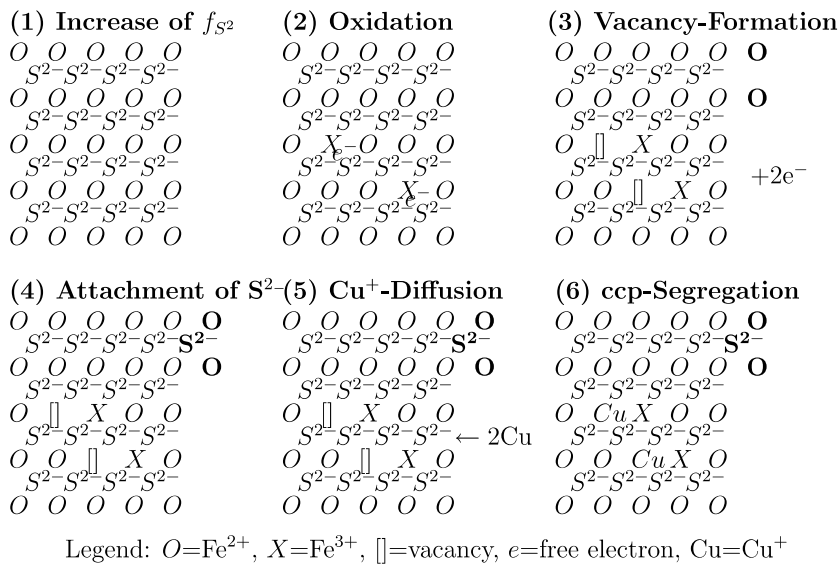


Figure 2. Reorganization of ZnS lattice to chalcopyrite.

with copper diffusing into the Fe-containing sphalerite crystal to form chalcopyrite ($=CuFeS_2$). During the process, gas S^{2-} molecules become attached to the crystal surface. Since, roughly speaking, the formation of chalcopyrite phases can only take place after a sufficient amount of Cu has diffused into the matrix, the generic mechanism has been called *diffusion induced segregation* (DIS).

Figure 2 sketches the reorganization of the sphalerite lattice close to the crystal boundary, assuming a perfect structure without impurities. The migration of Zn is not displayed as it behaves contrary to the migration of Cu.

The mathematical analysis of chalcopyrite disease presented in this work is based on partial differential equations and a thermodynamical description and tries to understand the physics underlying these examinations with the goal of making simulations close to the ideal experimental conditions. The developed model represents chalcopyrite disease on a medium

spatial scale; the microstructure is not resolved. The main idea pursued in this paper is to insert expressions of the free energy gained from *ab initio* calculations into (standard) finite element computations.

The paper is organized in the following way. In section 2 the mathematical formulation is restated. The general numerical ansatz is explained in section 3. Section 4 explains the implementation details of the harmonic approximation. Section 5 uses quantum mechanical (QM) methods for the sphalerite and chalcopyrite structure for validation and for computing elastic constants. In section 6 a comparison between molecular dynamics (MD)-simulations and harmonic approximation is carried out. The structure dependence of the computed data is studied in section 7. Section 8 is devoted to the computation of the diffusion constant of Cu depending on the concentrations of the other constituents. The results of some numerical experiments are presented in section 9. We finish with a critical evaluation of the results.

2. Mathematical formulation

Readers not interested in the details of the mathematical formalism only need to understand the reduction in the concentration vector to three components (stated by $c_S \equiv 0.5$ and relation (1)), accept the definition of the free energy (equation (4)) and the formulation as diffusion problem (equation (5)) and then can proceed with section 3.

Let Ω be a (time-independent) domain in \mathbb{R}^D , $1 \leq D \leq 3$, containing the crystal. By $0 < T_0 < \infty$ we denote a stop time and by $\Omega_T := \Omega \times (0, T_0)$ a cylinder in space-time. $c_i = c_i(x, t)$ denotes the relative number of species i , $i \in \{1, 2, 3\}$ per available lattice point at time t and space point $x \in \Omega$, where we set

$$c_1 \approx \text{Fe}, \quad c_2 \approx \text{Cu}, \quad c_3 \approx \text{Zn}, \quad c_4 \approx \text{vacancies}.$$

c_1 satisfies $c_1 = N_{\text{Fe}}/N_{\text{Me}}$, where N_{Fe} is the number of Fe atoms and N_{Me} the number of metal ion sites. Similar relationships hold for c_2 and c_3 . We will not model the attachment of S molecules at the lattice surface and assume that the concentration of S is identically $c_S := 0.5$. Due to electric neutrality we postulate, see [3, 5],

$$c_4 = \frac{1}{2}c_1. \quad (1)$$

By mass conservation the concentration vector c thus fulfils

$$c = (c_1, c_2, c_3) \in \Sigma := \{(\tilde{c}_1, \tilde{c}_2, \tilde{c}_3) \in \mathbb{R}^3 \mid \tilde{c}_i \geq 0, \frac{3}{2}\tilde{c}_1 + \tilde{c}_2 + \tilde{c}_3 \equiv \frac{1}{2}\}.$$

The constitutive relation for the mass fluxes is assumed to be of the form

$$J_i = \sum_{j=1}^3 L_{ij} \nabla \mu_j, \quad 1 \leq i \leq 3. \quad (2)$$

This isotropic ansatz goes back to [29]. L , the mobility, is symmetric due to Onsager's reciprocity law and a positive semi-definite 3×3 tensor. Furthermore,

$$\mu_j = \frac{\partial f}{\partial c_j}$$

is the chemical potential. To simplify the existence theory we assume that L is positive definite. The total Helmholtz free energy density f consists of f_1 for chalcopyrite and f_2 for sphalerite. Hence, the two different phases or lattice orders are characterized by two different free energies and f is the convex hull of f_1 and f_2 .

The characterization of the phases is given within the framework of functions of bounded variation $BV(\Omega)$ (see [14, 35]). It is convenient to introduce the set

$$V := \{\tilde{\chi} \in BV(\Omega) \mid \tilde{\chi}(1 - \tilde{\chi}) = 0 \text{ a.e. in } \Omega\} \quad (3)$$

and choose for the free energy with a constant $\gamma > 0$ the convex-combination

$$F(c, \tilde{\chi}) := \int_{\Omega} \gamma |\nabla \tilde{\chi}| + \int_{\Omega} (\tilde{\chi} f_1(c) + (1 - \tilde{\chi}) f_2(c)). \quad (4)$$

The first integral $\int_{\Omega} \gamma |\nabla \tilde{\chi}|$ defines the (constant) surface energy.

To sum up, we are concerned with the following formulation.

Find the vector $c = (c_1, c_2, c_3)$ and χ such that in $\Omega \subset \mathbb{R}^D$ for $t > 0$

$$\partial_t c_i = \operatorname{div} \left(\sum_{j=1}^3 L_{ij} \nabla \mu_j \right), \quad i = 1, 2, 3, \quad (5)$$

$$\mu_i = \chi \frac{\partial f_1}{\partial c_i}(c) + (1 - \chi) \frac{\partial f_2}{\partial c_i}(c), \quad i = 1, 2, 3, \quad (6)$$

$$F(c, \chi) = \min_{\tilde{\chi} \in V} F(c, \tilde{\chi}), \quad (7)$$

with the initial and boundary conditions

$$c_i(x, 0) = c_{0i}(x), \quad i = 1, 2, 3; \quad \chi(x, 0) = \chi_0(x) \text{ in } \Omega, \quad (8)$$

$$\left. \begin{array}{l} \partial_\nu \chi = 0, \\ c_i = g_i, \quad 1 \leq i \leq 3 \\ \mu_i = h_i, \quad 1 \leq i \leq 3 \end{array} \right\} \quad \text{at } \partial\Omega. \quad (9)$$

We stress that (7) actually means that the free energy is in a *global* minimum with respect to χ . For most physical systems, this assumption is not reasonable. But here the segregation dramatically changes the local lattice order such that there is a huge start energy and at least approximately a global minimum is obtained. If we replace (7) by an Allen–Cahn equation, the system may get stuck in a local minimum and flipping over from sphalerite to chalcopyrite may become impossible at large times t ; see the detailed discussion in [7].

The following theorem is covered by the results in [6]. It is formulated for classical Dirichlet boundary conditions $g_i = h_i = 0$.

Theorem 1 (Global existence of solutions for systems (5)–(9)). *There exists a weak solution (c, μ, χ) of (5)–(9) such that*

- (i) $c \in C^{0, \frac{1}{4}}([0, T_0]; L^2(\Omega; \mathbb{R}^3))$,
- (ii) $\partial_t c \in L^2(0, T_0; (H_0^1(\Omega; \mathbb{R}^3))')$,
- (iii) $\mu \in L^2(0, T_0; H_0^1(\Omega; \mathbb{R}^3))$,
- (iv) $\chi \in L^1(0, T_0; BV(\Omega))$ with $\chi(1 - \chi) = 0$ almost everywhere in Ω .

In general the solution (c, μ, χ) is not unique since χ may not be unique.

3. General outline of the numerical solution ansatz

We solve the weak formulation of (5)–(9) with linear finite elements. The arising discrete system is solved with a Newton–Krylov method. This is a quasi-Newton scheme where the inner linear loop is solved with the generalized minimal residual method (GMRES). This combines fast convergence of Newton’s method with the excellent damping properties of GMRES; see the extensive analysis in [9].

The various possibilities to speed up the finite element code such as parallelization by multi-grid methods or domain decomposition are not exploited. In order to incorporate approximations of the physical free energy, we will pursue the following ansatz. Let c be a given concentration vector. In a first independent computation step two approximations

$f_1^{\text{tab}}(c)$ and $f_2^{\text{tab}}(c)$ are computed which simulate the actual free energy density of the material in the bulk phases and hence represent two local minima of f . The main computational tool is the *harmonic approximation* with GULP [16], and the tabulated values $f_1^{\text{tab}}(c)$, $f_2^{\text{tab}}(c)$ are obtained from modified chalcopyrite and sphalerite configurations. Furthermore we apply MD simulations with DLPOLY (http://www.cse.clrc.ac.uk/msi/software/DL_POLY/). For QM computations we use ABINIT [18], a package originally developed by the Université Catholique de Louvain (<http://www.abinit.org>).

Generally, $f_1^{\text{tab}}(c)$ and $f_2^{\text{tab}}(c)$ are stored beforehand in huge databases. Each entry in these databases is a reference to a small range of concentration vectors c (approximation of f_i^{tab} by piecewise constant functions).

It remains to find approximations for $(\partial f_m^{\text{tab}})/(\partial c_j)$. This is done by central differencing of the tabular entries where possible and by one sided differences at the beginning and end of the database. To make this precise, let $M_j \in \mathbb{N}$ be the dimension of the database w.r.t. c_j , that is $f_m^{\text{tab}}(c_1, \dots, c_j, \dots, c_3)$ is constant for $c_j \in [c_j^l, c_j^{l+1})$ (c_j^l is a monotone sequence in l) and $1 \leq l \leq M_j - 1$. Set for $c_j \in (c_j^l, c_j^{l+1})$ (where we suppress the frozen components c_α for $\alpha \neq j$)

$$\frac{\partial f_m^{\text{tab}}}{\partial c_j}(c_j) := \begin{cases} \frac{f_m^{\text{tab}}(c_j^{l+1}) - f_m^{\text{tab}}(c_j^{l-1})}{c_j^{l+1} - c_j^{l-1}} & \text{if } 2 \leq l \leq M_j - 1, \\ \frac{f_m^{\text{tab}}(c_j^1) - f_m^{\text{tab}}(c_j^2)}{c_j^1 - c_j^2} & \text{if } l = 1, \\ \frac{f_m^{\text{tab}}(c_j^{M_j}) - f_m^{\text{tab}}(c_j^{M_j-1})}{c_j^{M_j} - c_j^{M_j-1}} & \text{if } l = M_j. \end{cases} \quad (10)$$

After numerical tests with analytic expressions for f , the parameters $M_1 = M_3 = 30$, $M_2 = 40$ were chosen. Larger values of M_j are desirable as they reduce the approximation errors. Unfortunately, the numerical effort grows enormously because every entry is the result of a costly averaging process as we shall see.

4. Free energy computation with GULP

The theory of harmonic approximation is explained in [2, 12]. For computations within GULP we have to fit the heuristic potentials that represent the short-range interatomic potentials. We begin with ZnS. We use the *Buckingham potential*

$$\phi(r) := -4\varepsilon(\sigma/r)^6 + B \exp(-r/\rho) \quad (11)$$

which gives in practice better results than Lennard–Jones potentials. In (11), r is the interatomic distance, σ that particular interatomic distance where the energy vanishes and ε is the potential energy at equilibrium separation. The term $(\sigma/r)^6$ describes the van-der Waals induced dipole moments whereas the exponential stands for the repulsive forces.

We use a shell model [11], where the rigid atom is split into an inner part comprising the nucleus with tightly bound inner electrons and an outer part with loosely bound shell electrons. This allows us to take dipole moments into account caused by the interactions with neighbouring ions. Additionally, a harmonic three-body potential is used to account for the directionality on the S–Zn–S bond according to the Taylor expansion

$$W_{3b}(\theta) := \frac{1}{2}k_2(\theta - \theta_0)^2 + \frac{1}{6}k_3(\theta - \theta_0)^3 + \frac{1}{12}k_4(\theta - \theta_0)^4,$$

where θ_0 is the angle of the unstressed three-body system and k_2 , k_3 and k_4 determine the sensibility w.r.t. angular changes; see [32] for details.

Table 1. Comparison of experimental and calculated data for ZnS.

	EXP1	EXP2	P1	P2	P3
$a/\text{\AA}$	5.41	5.41	5.403	5.403	5.402
$V/\text{\AA}^3$	158.29	158.29	157.77	157.77	157.69
C_{11}/GPa	9.42	9.76	8.6	9.37	9.18
C_{12}/GPa	5.68	5.9	6.54	6.16	5.83
C_{44}/GPa	4.36	4.51	3.8	4.03	4.41
$\varepsilon_{\text{stat}}$	7.9	—	8.565	7.21	7.33
ε_{hf}	5.8	—	4.815	4.56	3.64

Table 2. Potential parameters for P1, P2 and P3 used for ZnS.

	P1	P2	P3
Potential parameters			
S–S			
A/eV	1200.0	1200.0	1200.0
$\rho/\text{\AA}$	0.149	0.149	0.149
$B/\text{eV \AA}^6$	120.0	120.0	120.0
Zn–S			
A/eV	613.36	613.36	528.9
$\rho/\text{\AA}$	0.399	0.399	0.411
$B/\text{eV \AA}^6$	0.0	0.0	0.0
Shell model			
$\text{SK}_S/\text{eV \AA}^{-2}$	12.7	12.7	16.86
$\text{ZnK}_S/\text{eV \AA}^{-2}$	0.0	0.0	2.181
Three-body terms			
S–Zn–S force constant/ eV rad^{-2}		0.713	0.713
S–Zn–S bond angle/degrees		109.47	109.47
$k_2/\text{eV rad}^{-2}$		3.0	3.0
$k_3/\text{eV rad}^{-3}$		3.0	3.0
$k_4/\text{eV rad}^{-4}$		5.0	5.0

GULP sets up interactions of potentials between shells and other atoms/shells and these potentials must be fitted to give reasonable results. For sphalerite and chalcopyrite this is a tricky business, probably because the bondings in sulphides are not purely ionic but may range from ionic to covalent through to metallic. A least squares fit to measured parameters in the spirit of [34] is carried out (table 1). a is the lattice parameter of the cubic lattice, V the volume of the unit cell, C_{il} the elastic constants. To find the potential parameters, one starts with a simple model without shells where the charges of S and Zn are fixed to -2 and $+2$. By a least squares optimization run the parameters for the spring constant and in the case of sphalerite for the S–Zn–S interactions are fitted. The parameters thus obtained are then used in an extended model that includes shells and three-body terms.

For P1, a Buckingham potential is fitted and a shell is only used for the S ions. In P2, a three-body potential for S–Zn–S is added. In particular this results in better values of C_{44} , ε_{hf} and ε_{st} . In P3 a shell for Zn is included. The necessary parameters for a complete definition of the potentials are given in table 2. For all the Buckingham potentials, the cutoff level was set to 12 \AA .

The potentials P1 and P3 correspond to PS1 and PS3 in [34]. Some of the values in table 1 differ slightly from the figures reported there because all computations were redone with the

Table 3. Experimental/QM and calculated data for chalcopyrite.

	Exp2/QM	P4	P5
$a/\text{\AA}$	5.2864	5.601	5.59
$b/\text{\AA}$	5.2864	5.601	5.59
$c/\text{\AA}$	10.4102	10.71	10.70
$V/\text{\AA}^3$	145.46	168.08	167.73
C_{11}/GPa	17.83	18.02	18.12
C_{12}/GPa	5.81	5.67	5.64
C_{13}/GPa	6.27	6.59	6.59
C_{33}/GPa	13.15	14.23	14.25
C_{44}/GPa	13.19	18.86	18.93
C_{66}/GPa	4.93	8.68	8.70

newer version GULP 1.3. The data set EXP1 refers to the experimental results in [25] while EXP2 to the recently made measurements in [24] (in these experiments no measurements of $\varepsilon_{\text{stat}}$ and ε_{hf} were made).

As can be seen, the agreement documented in table 1 is suitably well with an error in the size of uncertainty of the measured parameters. This proves that GULP can be used to compute fundamental material properties of sulphides. P2 and P3 both seem to be very well suited to represent the structure of ZnS.

The fitting procedure to chalcopyrite is similar. For P4, Cu and Fe cores replace Zn. The S shell is fitted to yield good values for the lattice constants and the volume of the primitive cell. But there is one bottleneck: to date it has not been possible to measure the elastic parameters C_{ij} for chalcopyrite in experiment. The slanted parameters in table 3 are the result of QM computations in section 5 and the GULP potential is fitted to these parameters. To further improve the quality of the results, three-body potentials for S–Cu–S and S–Fe–S are added. Table 3 provides the results of the fitting and table 4 the fitting parameters.

We see that there is almost no improvement by using the three-body potentials. The agreement to the QM parameters is quite good, except for C_{44} and C_{66} .

5. QM computations

We perform QM computations on sphalerite and chalcopyrite using ABINIT [18]. The Born–Oppenheimer approximation of the Schrödinger equation is solved with the local-density approximation within the framework of density function theory [19, 20, 30]. For the representation of the electron–atom interactions Troullier–Martins pseudopotentials [33] are used.

After simple convergence tests, the energy cutoff e_{cut} was set to $20 \text{ Ha} \approx 544.23 \text{ eV}$ (one has $e_{\text{cut}} = \frac{1}{2}[2\pi(k + G_{\text{max}})]^2$ and G_{max} is the largest reciprocal lattice vector included in the Bloch expansion of the wave function) yielding a relative error of 0.4% in the total energy. The macroscopic dielectric constant $\varepsilon_{\text{diel}}$ of ZnS is preset to 8.32, the physical value found in the literature. For the self-consistent energy minimization cycle within ABINIT, the conjugated gradient method is chosen. In order to obtain satisfying results, the Brillouin zone is sampled with 182 k -points.

The following picture shows the binding energy for cubic ZnS as a function of a (figure 3).

The minimal value -7.22 eV is obtained at $a = 5.317 \text{ \AA}$ (the binding energy computed by GULP for $a = 5.419$ is -7.676 eV). A slight underestimation of the lattice constant and an overestimation of the binding energy are typical of well-converged local-density calculations.

Table 4. Potential parameters for P4 and P5 used for chalcopyrite.

	P4	P5
Potential parameters		
S-S		
A/eV	1200.0	1200.0
$\rho/\text{\AA}$	0.508	0.508
$B/\text{eV \AA}^6$	120.0	120.0
Fe-S		
A/eV	5694.68	5694.68
$\rho/\text{\AA}$	0.2748	0.2748
$B/\text{eV \AA}^6$	0.0	0.0
Cu-S		
A/eV	110.62	100.619
$\rho/\text{\AA}$	0.327	0.327
$B/\text{eV \AA}^6$	0.0	0.0
Shell model		
$SK_S/\text{eV \AA}^{-2}$	12.70	12.70
Three-body terms		
S-Cu-S force constant/ eV rad^{-2}	—	0.011 64
S-Cu-S bond angle/degrees	—	109.47
$k_2/\text{eV rad}^{-2}$	—	2.5
$k_3/\text{eV rad}^{-3}$	—	2.5
$k_4/\text{eV rad}^{-4}$	—	4.0
S-Fe-S force constant/ eV rad^{-2}	—	0.011 69
S-Fe-S bond angle/degrees	—	109.47
$k_2/\text{eV rad}^{-2}$	—	2.5
$k_3/\text{eV rad}^{-3}$	—	2.5
$k_4/\text{eV rad}^{-4}$	—	4.0

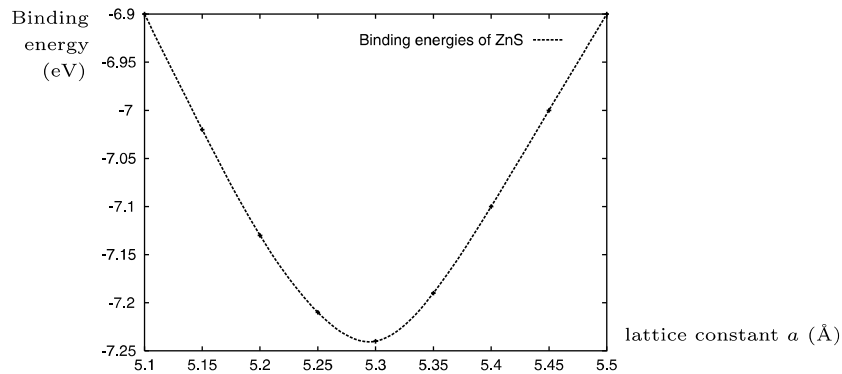
**Figure 3.** Binding energy in electronvolts for different lattice constants a and cubic ZnS.

Figure 4 displays the densities of state for cubic ZnS as a function of energy. The densities of state are computed using 182 k -points to cover the reciprocal lattice and with a tetrahedron method.

The computations for chalcopyrite are similar to those of ZnS. After convergence studies the energy cutoff e_{cut} was set to $30 \text{ Ha} \approx 816.35 \text{ eV}$ resulting in a relative error of 0.3%. Unfortunately, $\varepsilon_{\text{diel}}$ is unknown for chalcopyrite, so that for the first computations of the

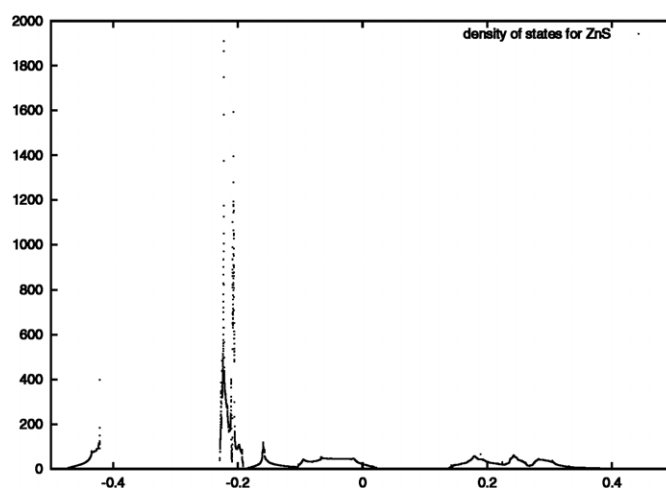


Figure 4. Density of states versus energy in Hartree ($1 \text{ Ha} \approx 27.211 \text{ eV}$) for ZnS.

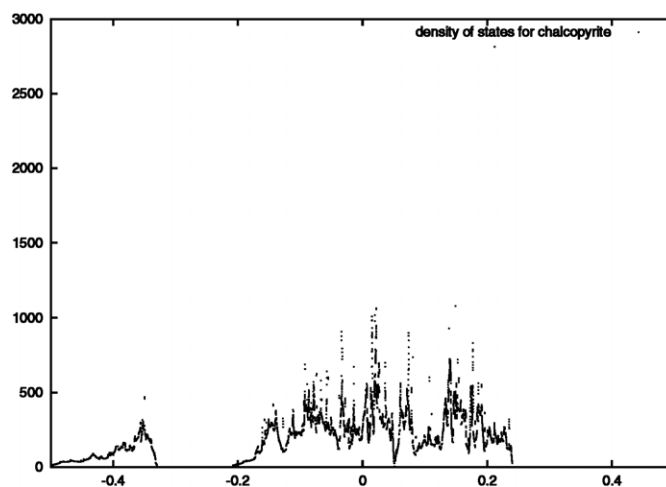


Figure 5. Density of states versus energy in Hartree for chalcopyrite.

relaxed geometry the ZnS-value is taken for chalcopyrite, too. Numerical tests have shown the results for chalcopyrite to change by less than 0.1% for different values of ϵ_{diel} . As in the case of sphalerite the Brillouin zone was sampled with 182 k -points. A not too small value is essential for the quality of the results.

Figure 5 displays the density of states for chalcopyrite. The minimal binding energy -19.7 eV is obtained at $a = b = 5.061 \text{ \AA}$ and $c = 9.969 \text{ \AA}$. The binding energy for chalcopyrite computed by GULP is -20.57 eV . Comparing with the lattice vectors computed by GULP, it appears probable that the constants a , b and c computed by DFT are as in the case of ZnS slightly too small.

In the rest of the section we compute C_{ij} via the acoustical modes. The obtained elastic constants are needed to gauge the interatomic potentials within GULP. The elastic constants for sphalerite serve as comparison and validation of the method.

Table 5. Comparison of experimental and calculated data for ZnS.

	EXP1	EXP2	QM	P2
$a/\text{\AA}$	5.41	5.41	5.32	5.403
$V/\text{\AA}^3$	158.29	158.29	150.36	157.77
B_0/GPa	76.6	—	82.8	71.55
C_{11}/GPa	9.42	9.76	9.63	9.37
C_{12}/GPa	5.68	5.9	5.89	6.16
C_{44}/GPa	4.36	4.51	4.87	4.03
$\varepsilon_{\text{stat}}$	7.9	—	—	7.21
ε_{hf}	5.8	—	—	4.56

Travelling waves in crystals (as waves in general) can be represented by

$$u(r, t) = \tilde{u} \exp(i(k \cdot r - \omega t)). \quad (12)$$

Here, u is the atomic elongation, $\tilde{u} = (\tilde{u}_1, \tilde{u}_2, \tilde{u}_3)$ the amplitude vector, $k = (k_1, k_2, k_3)$ the wave vector, $r = (r_1, r_2, r_3)$ the position vector and ω the angular frequency. The strain ε is given by

$$\varepsilon_{ij} = \frac{1}{2} \left(\frac{\partial u_i}{\partial x_j} + \frac{\partial u_j}{\partial x_i} \right). \quad (13)$$

With ABINIT we compute *dispersion curves*, i.e. curves which describe the relationship $k \mapsto \omega(k)$. More precisely we estimate with interpolation formulae the slopes $\omega'(0)$ of the acoustic phonon dispersion curves at the origin (acoustic phonon modes in contrast to optical phonon modes fulfil $\omega(k=0) = 0$). Using (12) in (13) yields

$$\varepsilon_{ij}(t) = \frac{i}{2} (u_i(t)k_j + u_j(t)k_i) = \frac{i}{2} (\tilde{u}_i k_j + \tilde{u}_j k_i) \exp(i(k \cdot r - \omega t)).$$

From Newton's equation of motion $\rho \partial_t^2 u_n = -\rho \omega^2 u_n$ we get

$$\rho \omega^2 \tilde{u}_n = \sum_{jlm} C_{njlm} k_j k_l \tilde{u}_m$$

or

$$\rho \omega^2 \tilde{u} = M(k) \cdot \tilde{u}.$$

The values on the left-hand side are provided by ABINIT. Suitable k -points can be gained by densifying the k -point mesh (with `dsifkpt`). It remains to compute the matrix M which is straightforward using the Voigt notation, see [28]. For the cubic ZnS lattice we find

$$M(k) = \begin{pmatrix} C_{11}k_1^2 + C_{44}(k_2^2 + k_3^2) & (C_{12} + C_{44})k_1k_2 & (C_{12} + C_{44})k_1k_3 \\ (C_{12} + C_{44})k_1k_2 & C_{11}k_2^2 + C_{44}(k_1^2 + k_3^2) & (C_{12} + C_{44})k_2k_3 \\ (C_{12} + C_{44})k_1k_3 & (C_{12} + C_{44})k_2k_3 & C_{11}k_3^2 + C_{44}(k_1^2 + k_2^2) \end{pmatrix}$$

and for tetragonal chalcopyrite it holds as

$$M(k) = \begin{pmatrix} C_{11}k_1^2 + C_{66}k_2^2 + C_{44}k_3^2 & (C_{12} + C_{66})k_1k_2 & (C_{13} + C_{44})k_1k_3 \\ (C_{12} + C_{66})k_1k_2 & C_{66}k_1^2 + C_{11}k_2^2 + C_{44}k_3^2 & C_{44}k_2k_3 \\ (C_{13} + C_{44})k_1k_3 & C_{44}k_2k_3 & C_{44}(k_1^2 + k_2^2) + C_{33}k_3^2 \end{pmatrix}.$$

Table 5 below shows the results of the computations for ZnS and extends the results of table 1. As before, EXP1 refers to the experimental results in [25], EXP2 to [24], PS2 to GULP results and QM is the quantum mechanical data. B_0 denotes the bulk modulus.

LDA tends to overbind and produces elastic constants larger than experiment.

Table 6 lists the results for chalcopyrite. The computed lattice constants are about 6% off the experimental values. Probably, the Troullier-Martins pseudopotentials are too soft.

The elastic constants found were used in section 4 to fit the GULP potentials.

Table 6. Comparison of experimental/calculated data for chalcopyrite.

	Exp2	QM	P5
$a/\text{\AA}$	5.2864	5.061	5.59
$b/\text{\AA}$	5.2864	5.061	5.59
$c/\text{\AA}$	10.4102	9.969	10.70
$V/\text{\AA}^3$	145.46	127.67	167.73
C_{11}/GPa	—	17.83	18.12
C_{12}/GPa	—	5.81	5.64
C_{13}/GPa	—	6.27	6.59
C_{33}/GPa	—	13.15	14.25
C_{44}/GPa	—	13.19	18.93
C_{66}/GPa	—	4.93	8.70

6. Analysis of the different parts of the entropy

Now we compare for certain reference configurations the results of the harmonic approximation and MD simulations. For a general introduction to MD simulations see for instance [15]. In particular this provides useful information as to how well the system entropy is captured. GULP can only compute the harmonic part of the system entropy. The anharmonic vibrational contributions to the system entropy are not captured.

For $T \approx 0$ K we will find that both methods yield almost identical results. Hence, one part of this section serves as a direct validation of MD and harmonic approximation. The used interatomic potentials are not verified by this comparison because they are the same in both applications (taken from tables 2 and 4).

Parameters of MD simulations (Keywords of DLPOLY) Cubic boundary conditions (imcon 1); overall 4000 steps, 2000 calibration steps, use of Berendsen thermostat with thermostat relaxation time 0.1 ps and barostat relaxation time 2 ps (ensemble npt berendsen 0.1 2), atom velocities are rescaled in every step (scale 1), ewald precision 10^{-6} , Verlet neighbour width 1 \AA (delr width 1 \AA); timestep 0.001 ps, pressure 0 kbar, cutoff 12 \AA ; the interatomic potentials are defined by table 2.

The results of DLPOLY are converted from the data of a $5 \times 5 \times 5$ supercell. The original data for sphalerite and $T = 0$ K is $\bar{a} = 27.1215 \text{\AA}$ and $\bar{F} = -16690 \text{ eV}$. In the last column, F is reconverted to $V_{\text{ref}} = 1000 \text{\AA}^3$, thereby taking into account the volume of the computed unit cell.

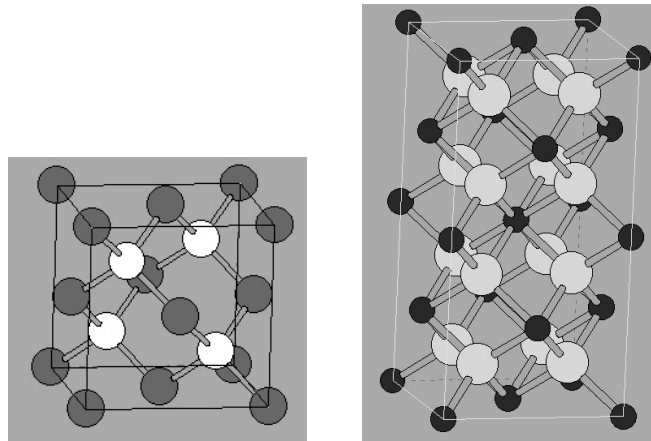
As can be seen, the agreement for $T = 0$ K (GULP only accepts $T > 0$ K for computations of the free energy) is extremely good when there is (almost) no entropic contribution to f . Further tests were made for selected atomistic configurations that arise during the phase transition from sphalerite to chalcopyrite again with a negligible difference in energy. We omit the presentation of the figures. This test is the afore-mentioned validation of GULP and DLPOLY.

Table 7 shows that chalcopyrite is energetically preferable; thus the lattice order of chalcopyrite is preferred if the concentration vector c permits it. We notice that the energy difference between GULP and DLPOLY data increases as T becomes larger. An increase in F for increasing T as stated by DLPOLY is plausible, and we conclude that GULP does not capture well the entropic part of F . Consequently, *computations based on DLPOLY may show a different behaviour from simulations based on harmonic approximation*. Though we expect this effect not to be decisive for the investigated temperature range as χ is determined by the global energy minimization (7) and the difference $F_1 - F_2$.

Table 7. Lattice geometry and free energy for GULP and DLPOLY.

Sphalerite	T	$a = b = c(\text{\AA})$	F (eV)	$F_{V_{\text{ref}}}$ (eV)
GULP	1 K	5.4243	-133.519	-836.58
	500 °C	5.4412	-135.37	-840.32
	700 °C	5.4473	-136.20	-842.61
DLPOLY	0 K	5.4243	-133.52	-836.59
	500 °C	5.4409	-132.72	-823.99
	700 °C	5.4493	-132.29	-817.53

Chalcopyrite	T	$a = b$ (Å)	c (Å)	F (eV)	$F_{V_{\text{ref}}}$ (eV)
GULP	1 K	5.577	10.68	-138.491	-832.63
	500 °C	5.598	10.701	-139.95	-832.08
	700 °C	5.606	10.705	-140.635	-835.85
DLPOLY	0 K	5.577	10.68	-138.493	-832.65
	500 °C	5.602	10.708	-139.09	-827.83
	700 °C	5.61	10.73	-139.37	-825.41

**Figure 6.** The unit cells of sphalerite and chalcopyrite.

7. The dependence of GULP data on atomistic lattice configurations

The concentration vector c determines the concentrations of Cu, Zn and Fe but not the position of the atoms within the lattice. It is clear that there is a large number of different configurations representing the same vector c and the free energy is in general different for these configurations. In order to take this issue into account, a supercell approach has been implemented in which all atoms are placed manually and no lattice symmetry is used *a priori*. The lattice unit cell is duplicated many times to fill the supercell and randomly certain atoms are replaced in order to fulfil the prescribed concentration percentage.

The following picture displays the three-dimensional lattice structure of cubic ZnS (space group $F\bar{4}3m$) and tetragonal chalcopyrite (space group $I\bar{4}2d$). In earlier work by Groß, the space group of chalcopyrite had wrongly been identified as $P\bar{4}2m$ but recent papers [21, 24] have it right.

From figure 6 we can read off the lattice transformation from sphalerite to chalcopyrite. The Zn atoms at the corners of the unit cell are replaced by Cu; the six Zn atoms at the centres

of every face are replaced by four Fe atoms and two Cu atoms. As the bonding energies change, the S atoms slightly shift their positions resulting in an overall change in the space group. In the direction of the lattice vector c of the unit cell, this corresponds to an almost doubling of the lattice constant.

From these considerations we can derive a natural replacement mechanism for the transformation from sphalerite to chalcopyrite (and vice versa). The positions where Cu atoms and Fe atoms are found in chalcopyrite determine those lattice points where Cu and Fe must be placed when altering the structure of sphalerite. The positions of the sulfur atoms are automatically adjusted during the minimization run of GULP.

The generation of the free energy databases requires the computation of two huge tables of the form $f_1^{\text{tab}}(c_i)$ and $f_2^{\text{tab}}(c_i)$ for *a priori* chosen concentration vectors c_1, \dots, c_N . For each vector c_i , many atomistic states c_i^α are automatically generated that all represent c_i on the supercell. As the number of atomistic states c_i^α representing c_i can be large and as it is not clear which of them are preferable, a file builder generates a certain number R_l of different GULP input files (R_l is chosen dynamically, with $20 \leq R_l \leq 100$, where $(f_l^{\text{tab}}(c_i^j))_{1 \leq j \leq 20}$ are always computed to sample the distribution), each with an atomistic configuration c_i^α , $1 \leq \alpha \leq R_l$, corresponding to the selected concentration vector c_i . For each input file, GULP is invoked and the table entries $f_l^{\text{tab}}(c_i^\alpha)$ are computed by the arithmetic mean

$$f_l^{\text{tab}}(c_i) := \frac{1}{R_l} \sum_{\alpha=1}^{R_l} f_l^{\text{tab}}(c_i^\alpha), \quad l = 1, 2.$$

The entire procedure is repeated for all c_i , $1 \leq i \leq N$, to build the two databases, $l = 1$ for chalcopyrite and $l = 2$ for sphalerite. For fixed c , the average values found represent the two minima $f_1^{\text{tab}}(c)$ and $f_2^{\text{tab}}(c)$.

Even though this method works out nicely, it has one disadvantage. Since all atoms are placed manually in the supercell (set up in accordance to the space group), GULP cannot use the lattice symmetry to accelerate the computations. Hence, the calculations are time consuming. For the generated database with discrete c values and partitions $M_1 = M_3 = 30$, $M_2 = 40$, the above calculations took 12 weeks of computations on a SUN workstation cluster.

For lattice geometry $l = 1, 2$ we want to analyse the variation in the free energies as computed by GULP for R_l atomistic configurations all of which represent one concentration vector. The aim is to find an empirical heuristic to control R_l .

Let c_i be the i th selected entry in the list of concentration vectors which is kept fixed in the following. Firstly, we compute admissible atom configurations c_i^j , $1 \leq j \leq 20$, of a $3 \times 3 \times 3$ supercell (for both lattice structures of sphalerite ($l = 2$) and chalcopyrite ($l = 1$)) which represent c_i , then invoke GULP to compute the free energies $f_l^{\text{tab}}(c_i^j)$, $l = 1, 2$. It is possible that $c_i^j = c_i^k$ for $j \neq k$ and $j, k \in \{1, 2, \dots, 20\}$, for instance, if only one atomistic configuration exists to represent c_i .

The values $(f_l^{\text{tab}}(c_i^j))_{1 \leq j \leq 20}$ are used to sample the distribution. We calculate the mean value (or expectation value)

$$\bar{f}_l := \frac{1}{20} \sum_{j=1}^{20} f_l^{\text{tab}}(c_i^j)$$

and the variance

$$s_l := \sqrt{\frac{\sum_{j=1}^{20} (f_l^{\text{tab}}(c_i^j) - \bar{f}_l)^2}{20}}.$$

Figure 7 shows the fraction s_l/\bar{f}_l for $l = 2$ of the sample $(f_2^{\text{tab}}(c_i^j))_{1 \leq j \leq 20}$ for different configurations of the sphalerite-supercell. s_2/\bar{f}_2 is plotted as a function of two arguments, the

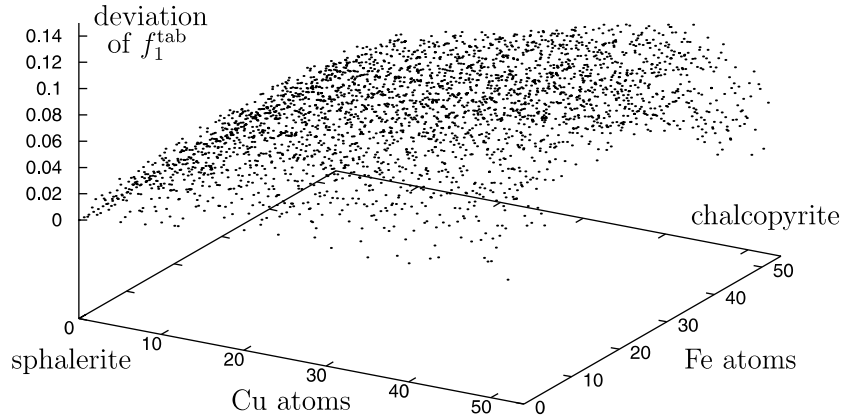


Figure 7. Deviation of GULP data for ZnS as a function of lattice configuration.

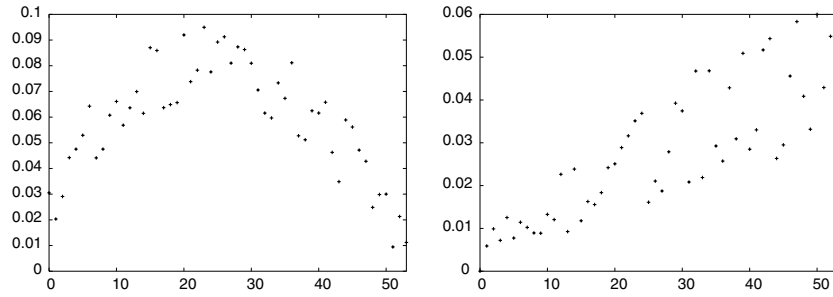


Figure 8. Cut through deviation data for $x = 45$ Cu atoms as a function of Fe atoms (left) and for $y = 45$ Fe atoms as a function of Cu atoms (right).

number of Cu atoms on the x -axis and the number of Fe atoms on the y -axis, both numbers being 0 and 54. As there are overall 108 positions which are not occupied by S atoms, the remaining are still filled by Zn. The lattice order of sphalerite is located at the origin ($x = y = 0$) of the diagram; the lattice order of chalcopryrite is placed at the right corner ($x = y = 54$). For these two geometries, the deviation of f_2^{tab} is exactly zero because only one atom configuration may be chosen.

From figure 7 we learn that the deviation of f_2^{tab} grows considerably stronger in the x direction than in the y direction indicating that the Cu atoms have a much larger impact on the geometry of the sphalerite-supercell than Fe.

The variation in f_1^{tab} is not displayed but is very similar to figure 7 with larger values as the superstructure of chalcopryrite almost doubles its length in the z direction. As the perspective in figure 7 may be misleading, two cuts through the graph are displayed in figure 8. The first is parallel to the y axis for $x = 45$ Cu atoms, the second parallel to the x -axis for $y = 45$ Fe atoms.

The information of the sample with 20 computed free energies is now used to estimate R_l . We assume that $X_l := (f_l^{\text{tab}}(c_i^j))_j$ is normally distributed where we put $\sigma_l := s_l$ for the variance in X_l . The transformed distribution $U_l := (X_l - \bar{f}_l)/\sigma_l$ has mean value 0 and variance 1. Now, for a given number $\rho > 0$, we determine a confidence interval of length ρ which contains \bar{f} with a probability of at least 95%. Let Φ denote the (tabulated) function of the normal distribution with variance 1 and mean value 0. In order to fulfil the 95% niveau and due to symmetry we

choose $u_0 := 1.96$ (we have $\Phi(u_0) \approx 0.975$). From the formula

$$|X_l - \bar{f}_l| \leq \frac{\rho}{2} = u_0 \frac{\sigma}{\sqrt{R_l}},$$

which implies $R_l := (4u_0^2\sigma^2)/\rho^2$, we infer the setting

$$R_l := \min \left\{ 100, \left\lceil \frac{4u_0^2\sigma^2}{\rho^2} \right\rceil \right\}.$$

The artificial cutoff value 100 is introduced to bound the computational effort.

8. Computation of the diffusion coefficient for Cu

The concentration of Cu governs the segregation process. The diffusion of Cu is nonlinear and depends on the concentrations of the other constituents and on the vacancies. In the following we perform computations to estimate this effect. Measured data is available for a perfect ZnS lattice in [26]. The reported figures predict $D_{\text{Fe}} \approx D_{\text{Cu}} \approx 10^3 \cdot D_{\text{Zn}}$ and $D_{\text{Cu}} = 2.6 \cdot 10^{-4} \text{ m}^2 \text{ s}^{-1}$. We use the measured constants D_{Zn} and D_{Fe} directly but need to analyse the dependence of D_{Cu} on the other constituents as this coefficient is crucial for the quality of the results.

We introduce the autocorrelation function of an arbitrary phase variable A by

$$\langle A \rangle := \frac{\int A(\Gamma) \exp(-\beta H(\Gamma)) d\Gamma}{\int \exp(-\beta H(\Gamma)) d\Gamma},$$

where $\Gamma := (r, p)$ is an element of the $6N$ -dimensional phase space, N the number of particles of the MD simulation, r the positions, p the momenta of the particles and $\beta := (k_B T)^{-1}$ with k_B the Boltzmann constant and H the Hamiltonian of the system. The computations are performed in the canonical ensemble; the temperature is preserved using the Nosé thermostat [27].

For the determination of the diffusion coefficient the relation

$$D_{\text{Cu}} = \frac{1}{6} \lim_{t \rightarrow \infty} \frac{d}{dt} \langle (r(t) - r(0))^2 \rangle \quad (14)$$

is fundamental. Equation (14) is an example of a Green–Kubo relation [17,22] and generalizes a result by Einstein [13].

Since D_{Cu} is a constant (for given c), (14) yields that $\langle (r(t) - r(0))^2 \rangle$ is asymptotically linear in t ; therefore

$$D_{\text{Cu}} = \frac{1}{6} \lim_{t \rightarrow \infty} \frac{\langle (r(t) - r(0))^2 \rangle}{t}. \quad (15)$$

Identity (15) relates the diffusivity of one selected Cu particle with the change in spatial coordinates of the same particle. The general diffusion coefficient $D_{\text{Cu}} = D_{\text{Cu}}(c)$ for the chosen concentration vector $c = (c_1, c_2, c_3)$ is computed by averaging over the diffusion coefficients of all particles.

Figure 9 plots D_{Cu} as a function of c . It shows that D_{Cu} increases for increasing Fe concentration as due to (1) the vacancy concentration increases, too. $c_2 \mapsto D_{\text{Cu}}(c)$ is decreasing, since in the physical process Zn must be replaced by Cu and leaves the crystal.

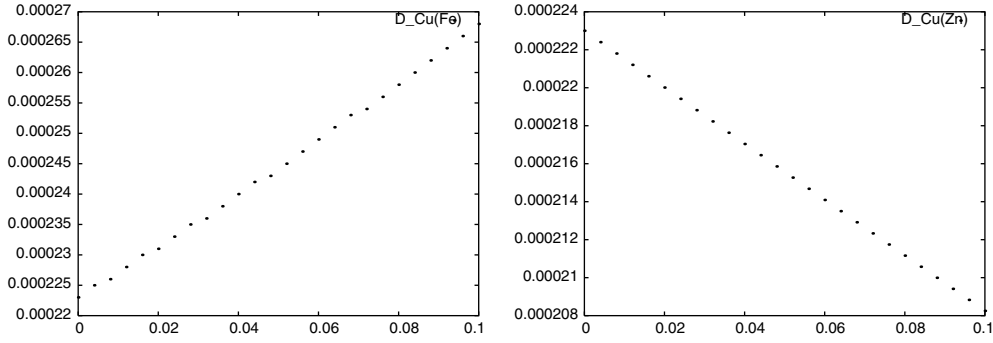


Figure 9. Functional dependence of D_{Cu} on Fe (left) and on Zn (right).

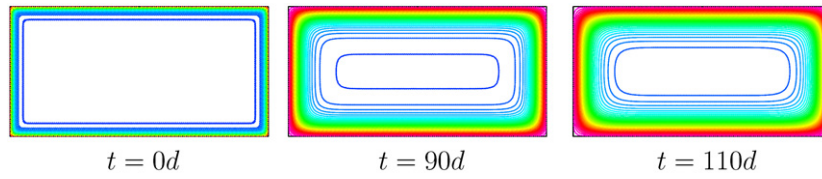


Figure 10. Diffusion of Cu. The density of the level sets indicates the steepness of the copper gradient. At $t = 0$, the initial datum falls from 0.25 at $\partial\Omega$ to 0.001 in Ω .

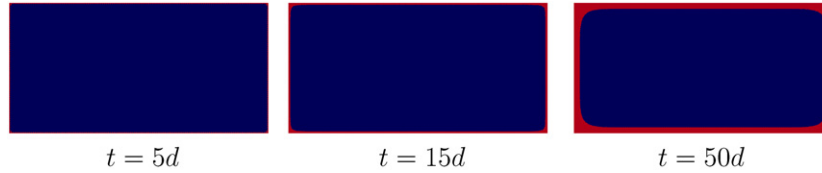


Figure 11. Segregation of chalcopyrite (red) within sphalerite (blue) in a perfect crystal as predicted by the harmonic approximation.

The computed value for D_{Cu} for a perfect crystal is $D_{\text{Cu}} \approx 2.23 \cdot 10^{-4} \text{ m}^2 \text{ s}^{-1}$ which does not coincide with the measured value $2.6 \cdot 10^{-4} \text{ m}^2 \text{ s}^{-1}$ in [26]. Therefore, we multiply any computed $D_{\text{Cu}}(c)$ by 1.15 in order to calibrate with the measurements.

9. Numerical results

Now we will focus on numerical solutions to systems (5)–(9) in its two-dimensional form based on the tabulated free energy and linear finite elements.

Figures 10 and 11 show the results of a finite element computation based on the tabulated harmonic free energy.

Physical parameters: $\Omega = [0, 0.2 \text{ m}] \times [0, 0.1 \text{ m}]$, $T = 500 \text{ }^\circ\text{C}$, $\gamma = 3 \cdot 10^{-9} \text{ m}$,
 D_{Cu} : Modified values of the constant $2.6 \cdot 10^{-4} \text{ m}^2 \text{ s}^{-1}$ as explained in section 8,
 $D_{\text{Fe}} \equiv 1.26 \cdot 10^{-4} \text{ m}^2 \text{ s}^{-1}$, $D_{\text{Zn}} \equiv 1.85 \cdot 10^{-7} \text{ m}^2 \text{ s}^{-1}$.
 Triangulation data: 33153 points, 65536 triangles, $h = 10^{-8}$.
 General parameters: $\epsilon_{\text{GMRES}} = \Delta t = 0.004$, $\eta = 10^{-8}$.

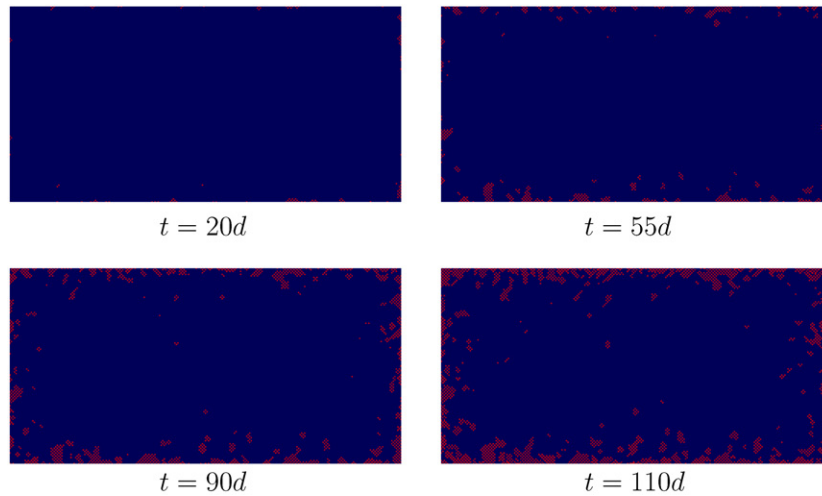


Figure 12. Time evolution of the chalcopyrite phase with small stochastic Fokker–Planck term in f_i . At $t = 0d$ only sphalerite (blue) is present (not displayed). As Cu enters from the boundary, chalcopyrite (red) forms. One can observe that the segregation starts with small islands that grow steadily.

Initial conditions: $c_{10} \equiv 0.066$, $c_{20} \equiv 0.001$ in Ω , χ_0 minimum of $\chi \mapsto F(c_0, \chi)$.

Boundary conditions: $\partial_\nu c_1 = \partial_\nu c_3 = \partial_\nu \chi = 0$ and $c_2 = 0.25$ on $\partial\Omega$.

Due to the boundary conditions, the Cu concentration increases in Ω during the computation. Once it exceeds a certain threshold, as a consequence of the free energy minimization (7), chalcopyrite (in red) is formed. The graph of Zn behaves contrary to that of Cu. The concentration of Fe is not displayed; it is a perfect constant in time and space.

At first glance it seems disappointing that figure 11 just shows a regular segregation front travelling inwards. But this result is clear due to symmetry: the initial values are constant in Ω and the parameters on which the diffusion coefficient D_{Cu} depends do not vary on the isolines displayed in figure 11.

As the experimental pictures of chalcopyrite disease within sphalerite suggest, there is a competition between the elastic energy and the surface energy. Yet, as we have just seen, there must be some mechanism which destroys the symmetry. Subsequently we assume that local changes arise in the free energy densities. These changes may be due to inhomogeneities of the material, and impurities in turn can be the seed for nucleation of chalcopyrite.

A stochastic source term in the context of spinodal decomposition has first been introduced by Cook [10]. Langer [23] has developed a statistical theory of spinodal decomposition leading to a Fokker–Planck equation. The stochastic source ξ is a white noise term and is added to the computed free energies by setting

$$f_1^{\text{st}}(c) = f_1^{\text{tab}}(c) + \xi(x, t), \quad f_2^{\text{st}}(c) = f_2^{\text{tab}}(c) - \xi(x, t), \quad (16)$$

where again $f_i^{\text{tab}}(c)$ denote the tabulated energies of the harmonic approximation and f_i^{st} are the free energy databases with stochastic component. Figure 12 visualizes the result of the computations with the stochastically perturbed free energy. We see that the solution looks very similar to the *in situ* observations and also predicts small chalcopyrite islands that proceed towards the main segregation front.

10. Discussion

We begin with a general evaluation of the employed *ab initio* techniques and list the problems that were encountered with these methods.

- No reasonable error estimates exist for the computed free energy as a function of the number of atoms in the numerical computation. It is clear that the asymptotic approximation of the calculated free energies towards some ‘limit’ as the number of atoms becomes large is only a prerequisite but not a proof of convergence.
- MD and harmonic computations can only compute states in electronic equilibrium. This is why electric equilibrium is assumed in the computations. Quantum effects are neglected for the generation of the free energy database as QM computations are very time consuming.
- The harmonic approximation does not capture well the vibrational parts of the entropy. As the analysis of section 6 reveals, the free energies computed with harmonic approximation and MD simulations may differ, and according to the formula $F = E - TS$ this effect increases as T increases. With the computer power available it was not possible to use MD simulations on a large scale the way the harmonic approximation is used in this work.
- The static and high frequency dielectric constants $\varepsilon_{\text{stat}}$ and ε_{hf} as well as the elastic constants of chalcopyrite are not known from experiment. At least the elastic parameters are needed to fit the GULP potentials. Therefore, the GULP potentials had to be fitted to QM computations in the hope that this provides satisfying data until experimental results are at hand.
- The numerical resolution of the finite element approach is quite poor when considering the spatial scale needed to satisfactorily resolve transition layers, nucleation centres and impurities.
- There exists no *a priori* justification of the density function theory; it can only be justified *a posteriori*. As for the other *ab initio* computations, no absolute bounds exist for the errors of the free energy approximations gained by QM computations. The problem of resolving the electron–electron interaction is already inherent in the Schrödinger equation itself which cannot be solved for three or more particles. Hartree–Fock models (with corrections of the correlation energy) do not seem to improve the situation.
- In simple cases, a renormalization of the frequencies, see [8] is possible, permitting the computation of the anharmonic part of the free energy. In more complicated situations, a thermodynamic integration between carefully chosen reference states as in [1] may be convenient.
- Assumptions are made on the geometry of the lattice during the phase transition. This means in particular that there is no intermediate lattice state with a different spatial geometry and that no other mechanisms (such as ‘wall pinning’ or polarons) play a role. More on this topic can be found in [31].
- In (7) the term $\int_{\Omega} \gamma |\nabla \chi|$ defines a constant surface energy. The correct physical surface energy F_S is not a constant but depends on c and on the atomistic configurations. In order to correctly compute F_S , pairs of atomistic configurations for both lattice geometries have to be plugged in and the surface energy has to be computed by averaging or by reasoning which configurations are unphysical. The implementation costs for this procedure are enormous.
- For practical implementation reasons, the numerical effort is limited and three artificial restrictions are introduced: the number of subdivisions M_j for the free energy databases in section 3, the size of the supercell in section 4 and the maximal number of computed

atomistic configurations per concentration vector (here 100) in section 7. Nothing is known about the impact of these bounds on the numerical solution (*finite size effects*).

For the GULP computations, a supercell as a conglomerate of $3 \times 3 \times 3$ unit cells is generated and only vectors c which are stoichiometric concentrations with respect to the supercell can be represented. This last restriction is not severe. There are 216 atoms within the $3 \times 3 \times 3$ supercell of sphalerite and 648 atoms within the larger supercell of chalcopyrite. Hence, c_1 and c_2 can be resolved for the supercell of sphalerite with $1/216 \approx 0.46\%$ and with $1/648 \approx 0.15\%$ for the supercell of chalcopyrite. Finally, the supercell geometry yields natural bounds for the concentrations $c_1, c_2 \leq 54/216 = 0.25$ and $c_3 \leq 0.5$.

A further note is required on the MD method. The number of atoms N of a computation is restricted by computer capacities and the numerical effort grows exponentially with N . A typical range for N is 10^3 – 10^6 atoms which is very far away from the *Avogadro number* $N_A = 10^{23}$. Despite this gap the method gives in practice surprisingly good results as long as $T > 100$ K. For low temperatures close to the zero point, quantum effects give large contributions and it is reasonable to see why the method yields wrong results. Yet, it is important to realize that whenever more than two atoms collide, there is no way to predict the velocities and momenta of these atoms *after* the collision. No reliable estimates are known for the number of collisions of triples (quadruples, quintuples, . . .) of atoms.

Finally, some remarks are in place about the limitations of the mathematical model for chalcopyrite disease within sphalerite.

- The ansatz does not cover the smallest length scales. No attempt is made to resolve the microstructure or the early stages of the nucleation of chalcopyrite within sphalerite.
- Impurities by other elements such as indium or selen are not taken into account.
- The attachment of S^{2-} ions and the growth of the crystal surface is not incorporated. A generalized model for the time-dependent domain and the derivation of an existence result based on geometric measure theory is in preparation.
- The spatial distribution of the inhomogeneities is not purely random as was assumed for simplicity. Precise knowledge on the coupling of $\xi(x, t)$ to the concentration vector c would be very valuable to improve the accuracy of the predictions by the model.
- In the simulations of section 8, material inhomogeneities as impurities are not taken into account. Furthermore, these calculations assume that the ensemble is in equilibrium at $t = 0$. The external field that corresponds to the diffusion force heats the system; therefore, the thermostat is essential.

Little is known about the actual influence of impurities, but it is believed that they play a crucial role as nucleation centres in the early stages of segregation. The mathematical models of homogeneous nucleation are not yet satisfying and further research in this direction (e.g. by analysing many-particle-models of Ising type) will hopefully yield some progress.

The main question concerning chalcopyrite disease within sphalerite is that of the underlying key mechanism. The first possibility is that the phenomenon is caused by inhomogeneous diffusion; the second option is that it is due to nucleation. If the diffusion coefficients behave in reality as suggested by the computations in section 8 (that exclude inhomogeneities) then the numerical results of section 9 indicate that diffusion as a responsible mechanism must be ruled out.

To summarize, a quantitative model for DIS is developed in this paper. The simulations capture the main properties of DIS. With the exception of metals where it is known that QM effects cannot be neglected and the harmonic approximation fails and yields wrong answers, the presented approach for chalcopyrite disease within sphalerite can be transferred to simulate other phenomena of solid state physics.

References

- [1] Alfe D, Price G D and Gillan M J 1999 *Nature* **401** 462–4
- [2] Ashcroft N W and Mermin N D 1976 *Solid State Physics* (Saunders College Publisher)
- [3] Bente K and Doering T 1993 *Eur. J. Mineral.* **10** 465
- [4] Bente K and Doering T 1995 *Miner. Petrol.* **53** 285–305
- [5] Blesgen T, Luckhaus S and Bente K 2002 *Cryst. Res. Technol.* **37** 570–80
- [6] Blesgen T 2005 *J. Math. Phys.* DOI 10.1063/1.1840292 022702-1–022702-29
- [7] Blesgen T, Luckhaus S and Bente K 2004 *Cryst. Res. Technol.* **39** 969–79
- [8] Blink R and Zeks B 1974 *Soft Modes in Ferroelectrics and Antiferroelectrics* (Amsterdam: North-Holland)
- [9] Brown P N 1987 *SIAM J. Numer. Anal.* **24** 407–34
- [10] Cook H E 1970 *Acta Metall.* **18** 297–306
- [11] Dick B G and Overhauser A W 1958 *Phys. Rev.* **112** 90–103
- [12] Dove M T 1993 *Introduction to Lattice Dynamics* (Cambridge: Cambridge University Press)
- [13] Einstein A 1905 *Ann. Phys.* **17** 549
- [14] Federer H 1996 *Geometric Measure Theory* (New York: Springer)
- [15] Frenkel D and Smit B 1996 *Understanding Molecular Simulation* (San Diego: Academic)
- [16] Gale J D 1997 *J. Chem. Soc. Faraday Trans.* **93** 629
- [17] Green M S 1954 *J. Chem. Phys.* **22** 398
- [18] Gonze X *et al* 2002 *Comput. Mater. Sci.* **25** 478–92
- [19] Hohenberg P and Kohn W 1964 *Phys. Rev. B* **136** 136
- [20] Kohn W and Sham L J 1965 *Phys. Rev. A* **140** 1133
- [21] Kratz T and Fuess H 1989 *Z. Kristall.* **186** 167–9
- [22] Kubo R 1957 *J. Phys. Soc. Japan* **12** 570
- [23] Langer J S 1975 *Ann. Phys.* **65** 53–86
- [24] Lepetit P, Bente K, Doering T and Luckhaus S 2003 *Phys. Chem. Miner.* **30** 185–91
- [25] Nickel E H 1965 *Information Circular IC 170* (Ottawa: Department of Mines, Technical Surveys)
- [26] Nelkowski P and Bollman S 1969 *Miner. Petrol.* **27**
- [27] Nose S and Klein M L 1983 *J. Mol. Phys.* **50** 1055
- [28] Nye J F 1964 *Physical Properties of Crystals* (Oxford: Clarendon)
- [29] Onsager L 1931 *Phys. Rev.* **37** 405–26
- [30] Payne M C, Teter M P, Allan D A, Arias T A and Joannopoulos J D 1992 *Rev. Mod. Phys.* **64** 1045–97
- [31] Salje E K H and Novak J 1998 *J. Phys.: Condens. Matter* **10** 359–66
- [32] Saunders M J, Leslie M and Catlow C R A 1984 *J. Chem. Soc.—Chem. Commun.* 1271
- [33] Troullier N and Martins J L 1993 *Phys. Rev. B* **43** 1991
- [34] Wright K and Jackson R 1995 *J. Mater. Chem.* **5** 2037–40
- [35] Ziemer W P 1989 *Weakly Differentiable Functions* (New York: Springer)